Thermally Tuning Terahertz Surface Plasmon Polaritons in Corrugated Semiconductor Films

Xin Wu, Ruwen Peng*, De Li, Ruili Zhang, Renhao Fan, Claudio Ferrari[1], and Mu Wang

National Laboratory of Solid State Microstructures and Department of Physics, Nanjing University, Nanjing 210093, China
[1]*IMEM-CNR Institute, Parco Area delle Scienze 37/A, Parma I-43010, Italy*

Received November 2, 2008; accepted January 18, 2009; published online April 20, 2009

In this work, we show that surface plasmon polaritons (SPPs) at terahertz (THz) frequencies can be tuned by changing the temperature in a periodically corrugated thin film of indium antimonide (InSb) sandwiched between air and dielectric. When a THz electromagnetic wave illuminates the structure, the temperature-dependent THz SPPs can be excited, and the first and second-order modes and their cross-couplings are observed in the band structure of SPPs. Reflection dips and transmission resonances are observed in those modes. By increasing temperature, transmissions decrease and reflections increase significantly. Our studies indicate that such effects may have potential applications in designing thermally controlled THz devices.

DOI: 10.1143/JJAP.48.042302

1. Introduction

Surface plasmon polaritons (SPPs) are collective electromagnetic excitations existing at the interface between a conductor and a dielectric.[1)] It is well known that SPPs are responsible for surface-enhanced Raman scattering in metallic nanosystems[2)] and extraordinary optical transmission through nanohole arrays in metal films.[3–6)] To date, most investigations of SPPs have been focused on metal surfaces in visible and infrared regions. However, some semiconductors can also support SPPs at terahertz (THz) frequencies owing to the fact that the real parts of their permittivities become negative in the THz range. For example, the propagation of THz SPPs has been studied in groove arrays of indium antimonide (InSb).[7,8)] The THz-SPP-enhanced transmissions have also been observed in the slit surrounded by periodic grooves in silicon wafer during photo excitation.[9)] However, the investigations of THz SPPs are still very limited. On the other hand, THz technology bridges the gap between photonics and electronics, and provides a powerful tool to characterize semiconductors and biomolecules.[10)] Moreover, THz spectroscopy and imaging may contribute to a wide range of applications in biology and medicine.[11–14)] Therefore, in depth research on THz SPPs will improve THz sensing and imaging.

In this work, we theoretically studied the effect of THz SPPs on the transmission and reflection of a thin InSb film with periodic corrugations when the film is illuminated by p-polarized THz electromagnetic waves. We showed that the THz SPPs are temperature-dependent, and the first and second-order modes and their cross-couplings are clearly shown in the SPP band structures. At those modes, reflection dips are found, and transmission resonances are observed as a transmission minimum or maximum. By increasing the temperature of the film, transmissions decrease and reflections increase significantly. Our investigation suggests that such InSb films may have potential applications in thermally controlled THz devices.

2. Theoretical Approach

To excite THz SPPs, we design the InSb film with periodic corrugations, sandwiched between the air and the dielectric

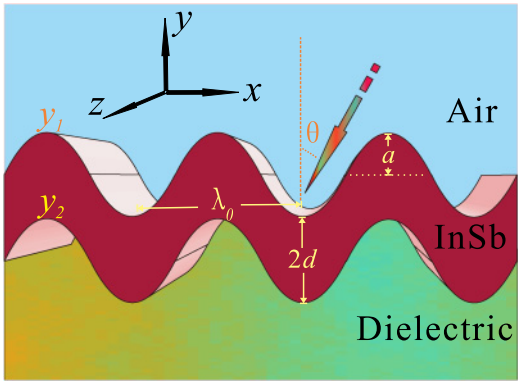

Fig. 1. (Color online) Geometry of the waved sandwich "air/InSb/dielectric" (AISD). The profiles of the sandwich shape are given by $y_1 = d + a\sin(k_g x)$ for the upper air/InSb interface and $y_2 = -d + a\sin(k_g x)$ for the lower InSb/dielectric interface at the xy plane. Here, $2d$ is the average thickness of the sandwich, a is the corrugation height, and $k_g = 2\pi/\lambda_0$ (λ_0 is the corrugation period). The two interfaces are assumed to be smooth and invariant in the z direction.

(as shown in Fig. 1). The profiles of the sandwich shape are given by $y_1 = d + a\sin(k_g x)$ for the upper air/InSb interface and $y_2 = -d + a\sin(k_g x)$ for the lower InSb/dielectric interface at the xy plane. Here, $2d$ is the average thickness of the sandwich, a is the corrugation height, $k_g = 2\pi/\lambda_0$ is the grating vector (or the corrugation vector) in the waved sandwich of "air/InSb/dielectric" (AISD), and λ_0 is the spatial period of the corrugation, as shown in Fig. 1. The THz electromagnetic wave illuminates the AISD at an incident angle θ. On the basis of the Rayleigh hypothesis,[15)] we theoretically investigated the propagation of an electromagnetic wave in the AISD. For a p-polarized incident wave (with its magnetic field in the z direction), the magnetic fields in three media of the AISD are expressed as Rayleigh expansions[16)] in terms of spatial harmonics as

$$H_{1z} = e^{i(\gamma_0 x - \beta_0 y)} + \sum_n B_{1n} e^{i(\gamma_n x + \beta_n y)} \qquad (y > y_1),$$
$$H_{2z} = \sum_n e^{i\gamma_n x}(A_{2n} e^{-i\beta_{2n} y} + B_{2n} e^{i\beta_{2n} y}) \qquad (y_1 < y < y_2), \quad (1)$$
$$H_{3z} = \sum_n A_{3n} e^{i(\gamma_n x - \beta_{3n} y)} \qquad (y < y_2).$$

Here, we assume that the incident amplitude is unity, and that B_{jn} $(j = 1, 2)$ and A_{jn} $(j = 2, 3)$ are the nth-order

*E-mail address: rwpeng@nju.edu.cn

reflection and transmission amplitudes, respectively, in the jth medium of the AISD. The wave vectors in eq. (1) are given by

$$\gamma_0 = k_0\varepsilon_{\text{air}}^{1/2}\sin\theta, \quad \gamma_n = \gamma_0 + nK, \quad k_0 = \omega/c,$$
$$\beta_n^2 = k_0^2\varepsilon_{\text{air}} - \gamma_n^2, \quad \beta_{2n}^2 = k_0^2\varepsilon - \gamma_n^2, \quad \beta_{3n}^2 = k_0^2\varepsilon_{\text{d}} - \gamma_n^2, \quad (2)$$

where k_0 is the free space wave vector, γ_0 and γ_n are the x components, and β_n, β_{2n}, and β_{3n} are the y components of the wave vector for the nth spatial harmonics in the three media. In addition, the boundary conditions in the AISD can be written as

$$H_{jz}|_{y=y_j} = H_{j+1,z}|_{y=y_j},$$

$$\left(\frac{1}{\varepsilon_j}\frac{\partial H_{jz}}{\partial n}\right)\bigg|_{y=y_j} = \left(\frac{1}{\varepsilon_{j+1}}\frac{\partial H_{j+1,z}}{\partial n}\right)\bigg|_{y=y_j}, \quad (3)$$

where $1/\partial n = [1 + (\partial y_j/\partial x)^2]^{-1/2}(\partial/\partial y - \partial y_j/\partial x \cdot \partial/\partial x)$ and $y_j = y_1$ or y_2 for the upper and lower interfaces, respectively. The permittivity $\varepsilon_j = \varepsilon_{\text{air}}$, ε, or ε_{d} for the three different regions in the AISD. When the two interfaces in the AISD have symmetrical profiles [$y_1 = d + a\sin(k_{\text{g}}x)$ and $y_2 = -d + a\sin(k_{\text{g}}x)$], an infinite set of coupled amplitude equations can be obtained from eqs. (1)–(3). At the air/InSb interface, the coupled amplitude equations[16] are written as

$$\sum_n [B_{1n}\exp(i\beta_n d)J_{m-n}(\beta_n a) - A_{2n}\exp(-i\beta_{2n}d) \times J_{n-m}(\beta_{2n}a) - B_{2n}\exp(i\beta_{2n}d)J_{m-n}(\beta_{2n}a)] = (-1)^{m+1}\exp(-i\beta_0 d)J_m(\beta_0 a), \quad (4)$$

and

$$\sum_n \left[B_{1n}\frac{\gamma_n\gamma_m - k_0^2\varepsilon_0}{\beta_n}\exp(i\beta_n d)J_{m-n}(\beta_n a) + A_{2n}\frac{\varepsilon_0}{\varepsilon} \times \frac{\gamma_n\gamma_m - k_0^2\varepsilon}{\beta_{2n}}\exp(-i\beta_{2n}d)J_{n-m}(\beta_{2n}a) - B_{2n}\frac{\varepsilon_0}{\varepsilon} \times \frac{\gamma_n\gamma_m - k_0^2\varepsilon}{\beta_{2n}}\exp(i\beta_{2n}d)J_{m-n}(\beta_{2n}a)\right] = (-1)^{m+1}\frac{k_0^2\varepsilon_0 - \gamma_0\gamma_m}{\beta_0}\exp(-i\beta_0 d)_m(\beta_0 a). \quad (5)$$

At the InSb/dielectric interface, the coupled amplitude equations are given by

$$\sum_n [A_{2n}\exp(i\beta_{2n}d)J_{n-m}(\beta_{2n}a) + B_{2n}\exp(-i\beta_{2n}d)J_{m-n}(\beta_{2n}a) - A_{3n}\exp(i\beta_{3n}d)J_{n-m}(\beta_{3n}a)] = 0, \quad (6)$$

and

$$\sum_n \left[A_{2n}\frac{\varepsilon_{\text{d}}}{\varepsilon}\frac{k_0^2\varepsilon - \gamma_n\gamma_m}{\beta_{2n}}\exp(i\beta_{2n}d)J_{n-m}(\beta_{2n}a) + B_{2n} \times \frac{\varepsilon_{\text{d}}}{\varepsilon}\frac{\gamma_n\gamma_m - k_0^2\varepsilon}{\beta_{2n}}\exp(-i\beta_{2n}d)J_{m-n}(\beta_{2n}a) + A_{3n} \times \frac{\gamma_n\gamma_m - k_0^2\varepsilon_{\text{d}}}{\beta_{3n}}\exp(i\beta_{3n}d)J_{n-m}(\beta_{3n}a)\right] = 0. \quad (7)$$

Here, m takes all integer values between $-\infty$ and $+\infty$. The expansion

$$\exp[i\beta\sin(k_{\text{g}}x)] = \sum_p \exp(ipk_{\text{g}}x)J_p(\beta)$$

has been used, where the first Bessel function is expressed as J_p.

Next, we obtained the reflectivity and transmittivity in the AISD. We truncate the superposition of the spatial harmonics and solve the amplitudes B_{1n}, B_{2n}, A_{2n}, and A_{3n} in the coupled amplitude equations [eqs. (4)–(7)] for a given frequency ω and incident angle θ. Since the time-averaged energy flow $\mathbf{S} = \text{Re}(\mathbf{E} \times \mathbf{H}^*)/2$ can be determined in each medium, the reflection and transmission coefficients along the y direction can be obtained as

$$R(\omega,\theta) = \frac{\displaystyle\int_0^{\lambda_0} \text{Re}\left\{\left[\sum_n B_{1n}e^{i(\gamma_n x + \beta_n y_+)}\right]^*\left[\sum_n B_{1n}\beta_n e^{i(\gamma_n x + \beta_n y_+)}\right]\right\}dx}{\beta_0\lambda_0}, \quad (y_+ \gg y_1),$$
$$T(\omega,\theta) = \frac{\displaystyle\int_0^{\lambda_0} \text{Re}\left\{\left[\sum_n A_{3n}e^{i(\gamma_n x - \beta_{3n} y_-)}\right]^*\left[\sum_n A_{3n}\beta_{3n}e^{i(\gamma_n x - \beta_{3n} y_-)}\right]\right\}dx}{\beta_0\lambda_0}\frac{\varepsilon_{\text{air}}}{\varepsilon_{\text{d}}} \quad (y_- \ll y_2). \quad (8)$$

respectively. Here, y_+ and y_- are selected so that the reflection and transmission at the far field region can be calculated. On the basis of reflection and transmission data, dispersion maps are obtained.

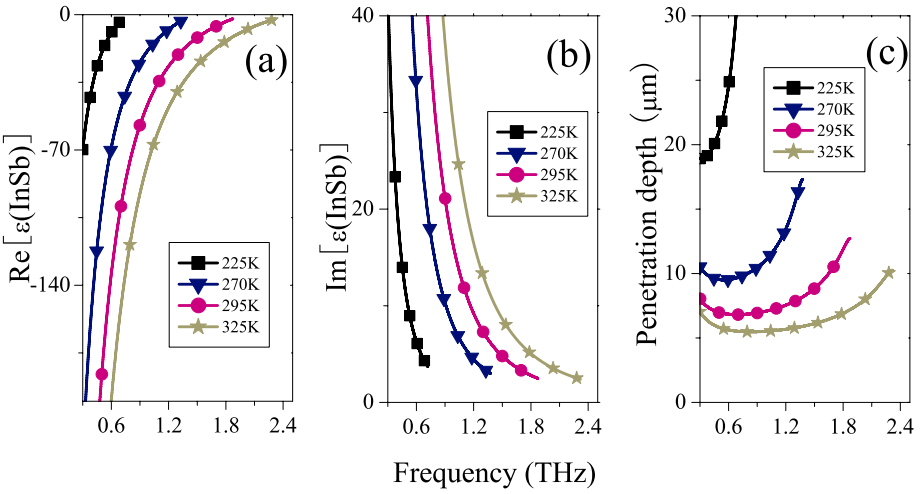

Fig. 2. (Color online) (a) Real and (b) imaginary parts of the permittivity for InSb based on eq. (9), and (c) the penetration depth of the THz wave into InSb for different temperatures. The square, triangle, circle, and star symbols indicate the values at temperatures of 225, 270, 295, and 325 K, respectively.

3. Numerical Calculations and Discussion

Because InSb has a high electronic mobility (about $7.7 \times 10^4\,\mathrm{cm^2 \cdot V^{-1} \cdot s^{-1}}$) and a small band gap (about 0.17 eV),[17] it is a promising candidate for applications in future high-performance and low-power transistors.[18] When the temperature varies from 225 to 325 K, there are many thermally excited carriers in InSb, which make InSb metallic at the THz region.[7,8] Thereafter, the dielectric functions of the InSb film are characterized by a Drude-type function

$$\varepsilon(\omega, T) = \varepsilon_\infty - \frac{\omega_p^2(T)}{\omega[\omega + i\Gamma(T)]}, \qquad (9)$$

where ε_∞ is the high-frequency permittivity, $\omega_p(T)$ is the plasma frequency, and $\Gamma(T)$ is the temperature-dependent collision rate. As shown in Figs. 2(a) and 2(b), the real part ($\mathrm{Re}\,\varepsilon$) and the imaginary part ($\mathrm{Im}\,\varepsilon$) of the permittivity of InSb at different temperatures are calculated on the basis of eq. (9) using the data in ref. 7. It is demonstrated that $|\mathrm{Re}\,\varepsilon|$ is larger than $\mathrm{Im}\,\varepsilon$ at THz frequencies, where InSb behaves as silver does at optical frequencies. Furthermore, the penetration depth of terahertz waves into InSb [$\delta_{\mathrm{InSb}} = |(\mathrm{Re}\,\varepsilon + \varepsilon_{\mathrm{air}})/(\mathrm{Re}\,\varepsilon)^2|^{1/2}/k_0$] is shown in Fig. 2(c) for different temperatures. The THz SPPs may be excited at the InSb/dielectric interface when it is illuminated by THz radiation and the resonant modes can be tuned by temperature. With consideration of the penetration depth for InSb at the THz band, an appropriate thickness of the InSb film should be chosen to observe resonant properties therein. As will be shown later, the reflection and transmission in some peculiar InSb films can be significantly affected by THz SPPs at temperature-tuned resonant modes.

On the basis of eqs. (4)–(8), we have calculated the reflectivity, the transmissivity, and the dispersion maps in the AISD. In the calculations, the parameters of the AISD are set as $\lambda_0 = 442.0\,\mu\mathrm{m}$, $d = 7.0\,\mu\mathrm{m}$, and $a = 28.7\,\mu\mathrm{m}$. The permittivities of the air and the dielectric are assumed to be $\varepsilon_{\mathrm{air}} = 1$ and $\varepsilon_{\mathrm{d}} = 2.13$, respectively. Loss in the dielectric is neglected. Obviously the Rayleigh hypothesis[19,20] is valid for our case.

The band structures of the THz SPPs in the AISD have been calculated at different temperatures. Figure 3 shows the dispersion maps of the THz SPP in the AISD based on reflection and transmission data for different incident angles at room temperature. It is obvious that the first and second-order air/InSb SPP branches are found in both the dispersion map corresponding to the reflection data [Fig. 3(a)] and that corresponding to the transmission data [Fig. 3(b)]. In addition, the InSb/dielectric SPP branches are also observed in the dispersion map shown in Fig. 3(b). The fields of the SPPs at the InSb/dielectric interface are too weak to be represented in the corresponding reflectivity dispersion maps. Furthermore, owing to periodic modulation in the AISD, the air/InSb SPPs with different orders can be coupled, whereas the air/InSb SPPs can also be coupled with the InSb/dielectric SPPs. As indicated in Figs. 3(a) and 3(b), five types of crossing points exist: (i) the crossing point of the $\pm$1st order air/InSb SPP modes (Point A_1); (ii) the crossing point of the $\pm$2nd order air/InSb SPP modes (Point A_2); (iii) the crossing points of the first order and the second order air/InSb SPP modes (Points B_1 and B_2), (iv) the crossing points of the first order InSb/dielectric SPP modes and the second order air/InSb SPP modes (Points C_1 and C_2), and (v) the crossing point of the $\pm$1st order InSb/dielectric SPP modes (Point D). (Point D is not distinguished for the AISD with the indicated parameters because the magnitudes of the $\pm$1st order InSb/dielectric SPP modes are very weak.) Usually, the coupling of SPPs leads to a band gap in an infinite periodic structure. However, no SPP band gaps can be found at the crossing points in the AISD, which originates from the absence of perturbed components in the shape profile of the AISD and the conformal thickness of the semiconductor layer. This phenomenon is similar to the coupling of the visible photons in a thin corrugated silver film, as shown in ref. 21.

To demonstrate the excitation of the THz SPPs in the AISD, the field distributions of electromagnetic waves at some resonant modes have been calculated. Figure 4 shows the time-averaged magnetic field distributions at some crossing points. In Fig. 4(a), the field distribution of the

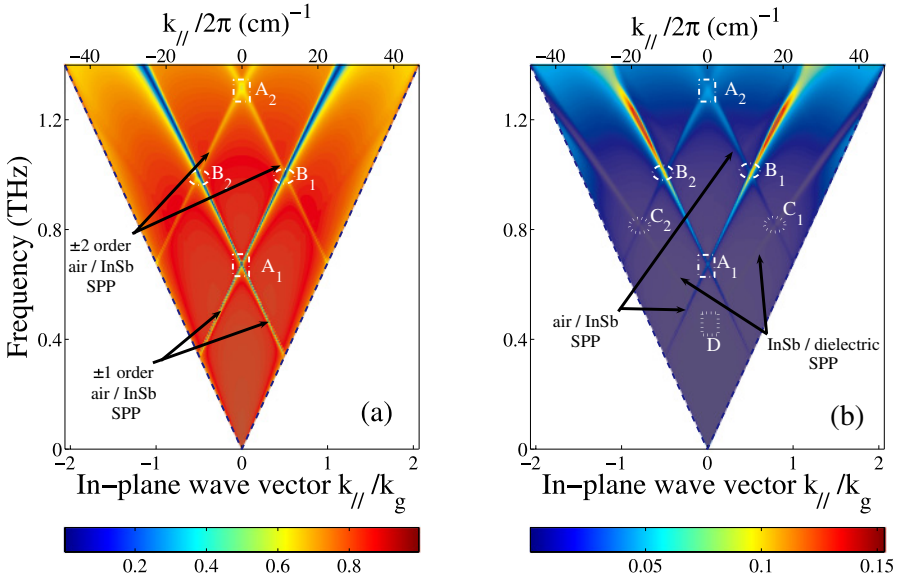

Fig. 3. (Color online) Dispersion maps of the THz SPP in the AISD based on (a) the reflection data and (b) the transmission data for different incident angles at room temperature $T \cong 295\,\mathrm{K}$. Here, the AISD is illuminated by p-polarized THz electromagnetic waves.

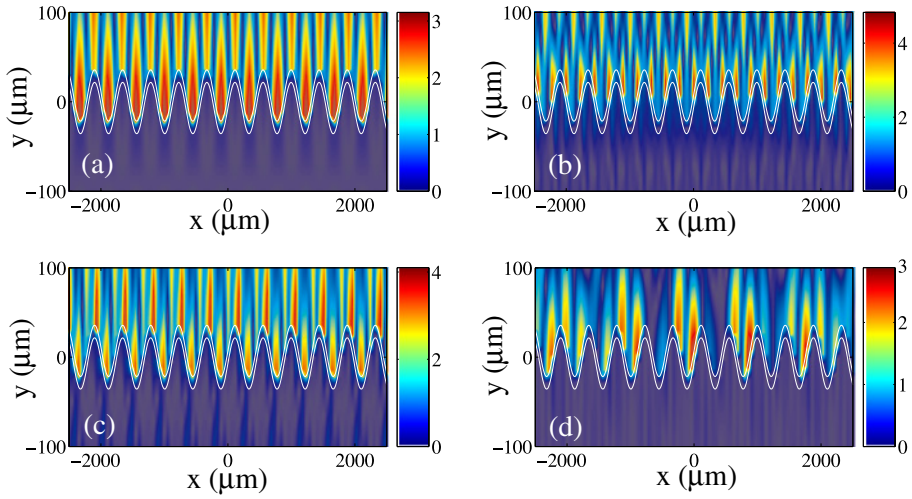

Fig. 4. (Color online) Time-averaged magnetic field H_z distributions at modes: (a) A_1, (b) A_2, (c) B_1 or B_2, and (d) C_1 or C_2. All these points are indicated in Fig. 3.

mode at Point A_1 (as indicated in Fig. 3) presents the same period of the AISD, i.e., λ_0, which agrees with the feature of the first order air/InSb SPP modes. In contrast, in Fig. 4(b), the field distribution of the mode at Point A_2 (as indicated in Fig. 3) is periodically distributed with a periodicity equal to $\lambda_0/2$, which is in good agreement with the feature of the second order air/InSb SPP modes. Figure 4(c) shows the field distribution of Point B_1 or B_2 (as indicated in Fig. 3), which exhibits the characteristics of both the first order and the second order air/InSb SPP modes. Similar periodic field distributions are found in Fig. 4(d) (Point C_1 or C_2 as shown in Fig. 3), except that the magnetic field from the air/InSb SPP mode is much stronger than that from the InSb/dielectric SPP mode, and the magnetic field exhibits a more complicated interference pattern.

Because the dielectric function of the InSb film is temperature-dependent, the excitation of the THz SPPs can be thermally tuned. This feature makes it possible to thermally change both the reflection and the transmission in the AISD. Figure 5 shows the temperature-dependent reflection and transmission spectra in the AISD for light incident at $\theta = 0^\circ$ (normal incidence) and $\theta = 10^\circ$ (oblique incidence). For both normal and oblique incidences, by increasing the temperature from 225 to 325 K, the InSb film presents gradually stronger metallic characteristics for a wider range of THz frequencies. Thereafter, the reflection and the transmission in the AISD appear a wider frequency range, and the reflection gradually increases [as shown in Figs. 5(a) and 5(c)] and the transmission decreases [as shown in Figs. 5(b) and 5(d)] at the same frequency.

The incident light is coupled to the THz SPPs in the AISD because the periodic corrugations provide compensational momentum. The THz SPPs are resonantly excited in the AISD, which occurs at the momentum

$$k_{\mathrm{SPP}} \equiv \frac{2\pi}{\lambda}\sqrt{\frac{\varepsilon_i \cdot \varepsilon(\omega, T)}{\varepsilon_i + \varepsilon(\omega, T)}} = k_{\parallel} \pm nk_{\mathrm{g}}. \qquad (10)$$

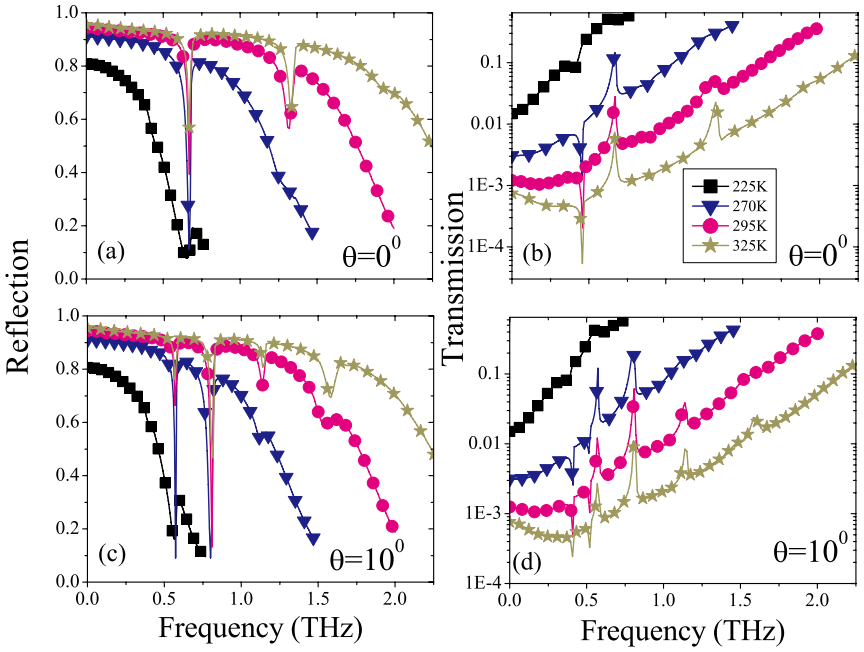

Fig. 5. (Color online) Calculated (a) reflection spectrum and (b) transmission spectrum at normal incidence, and the calculated (c) reflection spectrum and (d) transmission spectrum at an incident angle of $\theta = 10°$. The square, triangle, circle, and star symbols indicate the values at temperatures of 225, 270, 295, and 325 K, respectively.

Here, λ is the wavelength of incident light, ε_i represents the permittivity of the air or the dielectric, and $\varepsilon(\omega, T)$ is given by eq. (9). $k_\parallel$ is the in-plane wave vector, which is expressed as $k_\parallel = 2\pi \sin\theta/\lambda$, and k_g is the reciprocal lattice vector. At the resonant modes, the reflections are obviously suppressed, which leads to dips in the reflection. For example, at a temperature of 295 K, the reflection dips in Fig. 5(a) are observed at approximately 0.67 and 1.30 THz, which correspond to the first and second order air/InSb SPP modes in the AISD when the incidence is normal. Meanwhile, the resonant transmissions in Fig. 5(b) are observed as maxima at approximately 0.67 and 1.30 THz (the first and second order air/InSb SPP modes), or minima at approximately 0.45 and 0.90 THz (the first and second order InSb/dielectric SPP modes). The reason that the resonant transmission behaves either as a peak or a dip depends on the phase difference of the zero-order of transmitted light and the reradiated light from the SPP modes, which is affected by the film thickness. If the zero-order of transmitted light and the reradiated light from the SPP modes are in phase, maxima in transmission are observed. However, if these two components are in anti-phase, transmission minima are observed. Similar phenomena have been found in the periodically corrugated silver film at optical frequencies.[22] It is noteworthy that, in the THz band discussed in this paper, the absolute magnitude of the real part of $\varepsilon(\omega, T)$ is much larger than ε_i. Thereafter, the value of $\sqrt{\varepsilon_i \cdot \varepsilon(\omega, T)/[\varepsilon_i + \varepsilon(\omega, T)]}$ in eq. (10) is close to $\sqrt{\varepsilon_i}$. Hence the resonant modes only have a slight blue shift when the temperature is increased from 225 to 325 K. For example, the first order air/InSb SPP mode is shifted from 0.6515 THz at 225 K to 0.6696 THz at 325 K. Furthermore, when the incident angle becomes $\theta = 10°$ (oblique incidence), we find that each THz SPP mode at normal incidence is split into two modes [as shown in Figs. 5(c) and 5(d)], corresponding to the $+n$th order and the $-n$th order of THz-SPP resonances, respectively (n is an integer). This feature demonstrates that in the AISD, momentum matching between the light and the THz SPPs can be achieved by adding or reducing integer multiples of the grating vector k_g, which is in good agreement with the dispersion maps shown in Fig. 3.

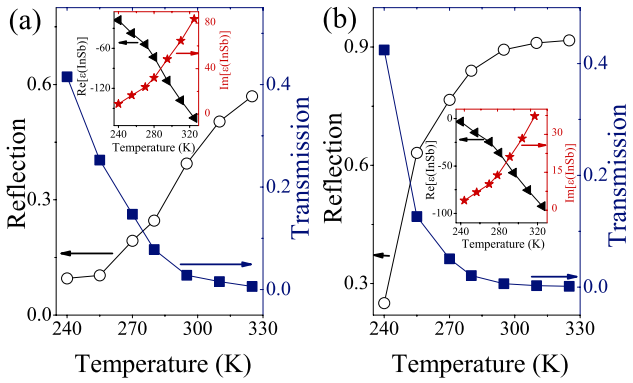

Fig. 6. (Color online) Temperature dependence of the reflection (hollow circles) and the transmission (solid squares) in the AISD, which is illuminated by (a) a 0.67 or (b) a 0.90 THz electromagnetic wave at normal incidence. The inset illustrates the real part (triangles) and the imaginary part (stars) of the permittivity of InSb as a function of temperature.

It is possible to tune the reflection and the transmission by changing the temperature in the AISD. Figures 6(a) and 6(b) show the temperature-dependent reflection and transmission spectra when the frequency of the normal incident electromagnetic wave is 0.67 and 0.90 THz, respectively. For the case in which the frequency of the incident wave is 0.67 THz (the frequency is around the first order air/InSb SPP mode), the reflectivity increases from 9.5 to 56.9% and the trans-

mission decreases from 41.5 to 0.6% when the temperature increases from 240 to 325 K [as shown in Fig. 6(a)]. When the frequency of the incident wave is 0.90 THz, the reflectivity increases from 25.0 to 92.0%, and the transmission decreases from 42.4 to 0.14% when the temperature increases from 240 to 325 K [as shown in Fig. 6(b)]. This feature originates from the fact that the permittivity of InSb is temperature-dependent (as shown in the inset of Fig. 6). Because the permittivity of InSb varies with temperature, the characteristics of THz SPPs can be thermally tuned in the AISD. Consequently, we may control the electromagnetic properties of THz devices based on AISDs by simply changing the temperature instead of by tuning the geometrical parameters of the structure.

4. Conclusions

On the basis of the Rayleigh hypothesis, we have studied the transmission and reflection spectra of AISDs affected by THz SPPs. From the coupled amplitude equations of electromagnetic waves, the reflectivity, the transmittivity, and the dispersion maps in the AISD are obtained. It is shown that, as temperature-dependent THz SPPs are excited, the first and second-order modes and their cross-couplings can be clearly identified in SPP band structures. At those resonant modes, the reflections are obviously suppressed, which leads to dips in the reflection; whereas the transmissions through the AISD can be observed as either minima or maxima, depending on the film thickness. By increasing the temperature of the InSb film, the transmissions decrease and the reflections increase significantly. This feature suggests that such InSb films may have potential applications in thermo sensitive THz devices.

Acknowledgments

This work was supported by grants from the National Natural Science Foundation of China (Grant Nos. 10625417, 50672035, and 10874068), the State Key Program for Basic Research from the Ministry of Science and Technology of China (Grant Nos. 2004CB619005 and 2006CB921804), and partially by the Ministry of Education of China and Jiangsu Province (Grant Nos. NCET-05-0440 and BK2008012). In addition, RHF thanks the National Fund for Fostering Talents of Basic Science (J0630316) for support.

1) H. Raether: *Surface Plasmons* (Springer, Heidelberg, 1988) p. 1.
2) H. S. Zhou, I. Honma, H. Komiyama, and J. W. Haus: Phys. Rev. B **50** (1994) 12052.
3) T. W. Ebbesen, H. J. Lezec, H. F. Ghaemi, T. Thio, and P. A. Wolff: Nature **391** (1998) 667.
4) W. L. Barnes, A. Dereux, and T. W. Ebbesen: Nature **424** (2003) 824.
5) C. Genet and T. W. Ebbesen: Nature **445** (2007) 39.
6) Z. H. Tang, R. W. Peng, Z. Wang, X. Wu, Y. J. Bao, Q. J. Wang, Z. J. Zhang, W. H. Sun, and Mu Wang: Phys. Rev. B **76** (2007) 195405.
7) J. A. Sánchez-Gil and J. Gómez Rivas: Phys. Rev. B **73** (2006) 205410.
8) J. Gómez Rivas, M. Kuttge, H. Kurz, P. H. Bolivar, and J. A. Sánchez-Gil: Appl. Phys. Lett. **88** (2006) 082106.
9) E. Hendry, F. J. Garcia-Vidal, L. Martin-Moreno, J. G. Rivas, M. Bonn, A. P. Hibbins, and M. J. Lockyear: Phys. Rev. Lett. **100** (2008) 123901.
10) B. Ferguson and X.-C. Zhang: Nat. Mater. **1** (2002) 26.
11) D. Wu, N. Fang, C. Sun, X. Zhang, W. J. Padilla, D. N. Basov, D. R. Smith, and S. Schultz: Appl. Phys. Lett. **83** (2003) 201.
12) D. Dragoman and M. Dragoman: Prog. Quantum Electron. **28** (2004) 1.
13) P. H. Siegel: IEEE Trans. Microwave Theory Tech. **52** (2004) 2438.
14) A. Battula, Y. Lu, R. J. Knize, K. Reinhardt, and S. Chen: Opt. Express **15** (2007) 14629.
15) L. Rayleigh: Proc. R. Soc. London, Ser. A **79** (1907) 399.
16) S. Dutta Gupta, G. V. Varada, and G. S. Agarwal: Phys. Rev. B **36** (1987) 6331.
17) O. Madelung: *Physics of III-V Compounds* (Wiley, New York, 1964) p. 3.
18) R. Chau, S. Datta, M. Doczy, B. Doyle, B. Jin, J. Kavalieros, A. Majumdar, M. Metz, and M. Radosavljevic: IEEE Trans. Nanotechnol. **4** (2005) 153.
19) T. Watanabe, Y. Choyal, K. Minami, and V. L. Granatstein: Phys. Rev. E **69** (2004) 056606.
20) T. Elfouhaily and T. Hahn: Phys. Rev. Lett. **97** (2006) 120404.
21) Z. Chen, I. R. Hooper, and J. R. Sambles: J. Opt. A **10** (2008) 015007.
22) I. R. Hooper and J. R. Sambles: Phys. Rev. B **67** (2003) 235404.